Phase transitions on a multiplex of swarmalators

Steve J. Kongni and Venceslas Nguefoue

Research Unit Condensed Matter, Electronics and Signal Processing, University of Dschang, P. O. Box 67 Dschang, Cameroon
and MoCLiS Research Group, Dschang, Cameroon

Thierry Njougouo

Faculty of Computer Science and naXys Institute, University of Namur, 5000 Namur, Belgium;
Namur Institute for Complex Systems (naXys), University of Namur, Belgium;
Department of Electrical and Electronic Engineering, Faculty of Engineering and Technology (FET),
University of Buea, P. O. Box 63, Buea, Cameroon;
and MoCLiS Research Group, Dschang, Cameroon

Patrick Louodop

Research Unit Condensed Matter, Electronics and Signal Processing, University of Dschang, P. O. Box 67 Dschang, Cameroon;
ICTP South American Institute for Fundamental Research, São Paulo State University (UNESP),
Instituto de Física Teórica, 01140-070 São Paulo, Brazil;
and MoCLiS Research Group, Dschang, Cameroon

Fernando Fagundes Ferreira

Center for Interdisciplinary Research on Complex Systems, University of Sao Paulo, São Paulo 03828-000, Brazil;
and Department of Physics-FFCLRP, University of São Paulo, Ribeirão Preto, SP 14040-901, Brazil

Robert Tchitnga

Research Unit Condensed Matter, Electronics and Signal Processing, University of Dschang, P. O. Box 67 Dschang, Cameroon

Hilda A. Cerdeira

São Paulo State University (UNESP), Instituto de Física Teórica, 01140-070 São Paulo, Brazil
and Epistemic, Gomez & Gomez Ltda. ME, 05305-031 São Paulo, Brazil

Dynamics of bidirectionally coupled swarmalators subject to attractive and repulsive couplings is analyzed. The probability of two elements in different layers being connected strongly depends on a defined vision range r_c which appears to lead both layers in different patterns while varying its values. Particularly, the interlayer static sync π has been found and its stability is proven. First-order transitions are observed when the repulsive coupling strength σ_r is very small for a fixed r_c and, moreover, in the absence of the repulsive coupling, they also appear for sufficiently large values of r_c. For $\sigma_r = 0$ and for sufficiently small values of r_c, both layers achieve a second-order transition in a surprising two steps that are characterized by the drop of the energy of the internal phases while increasing the value of the interlayer attractive coupling σ_a and later a smooth jump, up to high energy value where synchronization is achieved. During these transitions, the internal phases present rotating waves with counterclockwise and later clockwise directions until synchronization, as σ_a increases. These results are supported by simulations and animations added as supplemental materials.

I. INTRODUCTION

Describing the evolution of real living and/or material systems is a very interesting subject due to its importance in many fields such as epidemiology [1], chiral microswimmers [2], neuroscience [3,4], and so on [5,6]. Part of this objective has led many researchers to focus on the interactions between entities in different environments. These observations, which have been extended to the study of interactions among species such as humans, animals, and micro-organisms, have led to the establishment of mathematical models that can describe the dynamics of living or material systems or their ensembles [1,2,5]. Synchronization behaviors [7–13], aggregation or clustering [8,9,14–18], and chimeras states [9,19,20] have been observed and have led to many applications in science and technology.

Synchronization dynamics can be described as a state of coherent and identical behavior of interacting elements in a given environment. This phenomenon was first observed by the physicist Christiaan Huygens in mutually coupled periodic oscillators in 1673 [10]. Since then, various works have investigated this phenomenon in different particular situations [7–9,21–30].

Thus, in order to simulate these behaviors into real situations, systems that can describe collective displacement in space were developed and called mobile oscillators [17,31–35]. The extension of these works allowed us to define others that can synchronize and swarm when spatial and internal dynamics are coupled, and they were called swarmalators [14]. Several other works have allowed a partial understanding of swarmalator systems [15,16,18,36–38]. H. K. Lee *et al.* [38] investigated the steady-state patterns of population of swarmalators, where the interaction distances among the nodes have a finite cutoff sometimes named vision range [17]. Within their results, they found barlike patterns. G. K. Sar *et al.* [18] studied the swarmalators under time-dependent phase interactions. They found unknown asymptotic states, like static π, and mixed phase wave states under the double action of attractive-repulsive competitive phase couplings. This paper aims to combine both the use of the finite cutoff in the interaction distance and the combination of attractive and repulsive coupling in multilayer swarmalators.

Coupled systems show many behaviors within which one of the most impressive is the sudden and abrupt change that occurs as an explosive collective phenomenon called explosive synchronization [39,40]. The first-order transition has long been an intriguing behavior characterized by an abrupt phase change from an asynchronous to a synchronous state. In 2011, it has been argued that this phenomenon can happen when there is correlation between the natural frequency of the nodes of a network and their degree for scale-free network [39]. However, in Refs. [40,41] the authors showed that it is possible to obtain a first-order transition with no correlation between the natural frequency and the degree of the nodes. This result was also generalized in Refs. [42,43], where the authors investigated different mechanism to generate frustration with lead to abrupt transitions.

Moreover, this transition can be observed under the effect of a random coupling [44] or in the case of a perturbation (noise) on the natural frequency of the entities of a Kuramoto oscillator network [45]. This can also be observed in a multiplex and adaptive pair oscillator network [40]. In addition, the first-order transition to synchronization was also extended to multiplex networks of identical [46] or dissimilar layers [47] and to the combined effect of the natural frequency distribution and the interlayer delay [48]. The second-order transitions as well as the abrupt or explosive ones can be observed in some real systems such as a school of fish or a flocking bird evolution [49–53] or insects motions [54,55]. A review of their applications and roles in biological processes was done recently by E. F. W. Heffern *et al.* [56]. However, the chosen coupling topology can be a key element in achieving explosive synchronization [39,41,43] and many other phenomena such as chimeras states [57–60].

Within the many important issues in the theory of networks appears that of the influence that the interlayer interaction between elements has in the dynamics of multilayer networks. Several phenomena have been investigated as varied as showing the importance of the topology of the multiplex to obtain a second-order transition to synchronization [58,61,62] or the increase of the synchronization probability [8,60,62–65].

Apart from the importance that these studies have to understand all the states of the dynamics, there are examples where swarmalators dynamics may be useful to explain natural behaviors such as motile bacteria, when in close contact with surfaces, use a mechanism referred to as "swarming" to access new sources of nutrients [66]. Swarming colonies of bacteria show dynamics such as low curvature of trajectories, circular vortices, cooperative motility and alignment of cells, etc. [67]. Cells communication attenuates growth to control the organization of communities [68].

In an attempt to understand what the mobility of these systems may represent in nature here we study a two layer network of swarmalators, described by the model presented in Sec. II, where we analyze the influence that attractive and repulsive coupling have in the dynamics. We find a rich set of behaviors, including rotational behavior of the internal phases leading to synchronization.

This work has four main parts. From the present introduction in Sec. I, we present in Sec. II the model under study and schematic descriptions of the interactions between the two layers highlighting the vision range. In Sec. III, the analysis tools allowing the characterization of the obtained dynamics are described; meanwhile, Sec. IV presents the numerical results and the study of the stability between the two layers. Section V is devoted to the conclusion and some perspectives. Finally, in the Appendix, we present a glossary of the dynamical phases.

II. MODEL

We present a model for a system of oscillators whose phase and spatial dynamics are coupled used to describe the dynamics of some living systems, called swarmalators [14,16,18,37,69]. The generalized equations are given as follows:

$$\dot{X}_i = v_i + \frac{1}{N} \sum_{j \neq i}^{N} [F_{\text{att}}(X_j - X_i)W(\theta_j - \theta_i) - F_{\text{rep}}(X_j - X_i)],$$
(1)

$$\dot{\theta}_i = w_i + \frac{K}{N} \sum_{j \neq i}^{N} H_{\text{att}}(\theta_j - \theta_i)G(X_j - X_i),$$
(2)

with $i, j = 1, \ldots, N$, where N is the total number of swarmalators, θ_i is the phase of the internal dynamics of each element, $X_i = (x_i, y_i)^T$ is the spatial coordinate of the i_{th} entity, and v_i and w_i are the velocity and natural frequency of each element, respectively. Then the dynamics of the system is defined by the spatial angle ϕ describing the position given by $\phi_i = \arctan(y_i/x_i)$ and the coupled phase θ_i

In this model there are three explicit functions defined by F_{att}, H_{att}, and F_{rep} which respectively represent the attractive and repulsive interactions between entities in the network [14,16]. The competition between F_{att} and F_{rep} gives rise to clusters of particles with sharp boundaries, in agreement with many biological systems [36]. The functions W and G represent the influence that the internal dynamics have on the movement of the oscillators and vice versa. Thus, the model presented previously in Eqs. (1) and (2) can be rewritten as
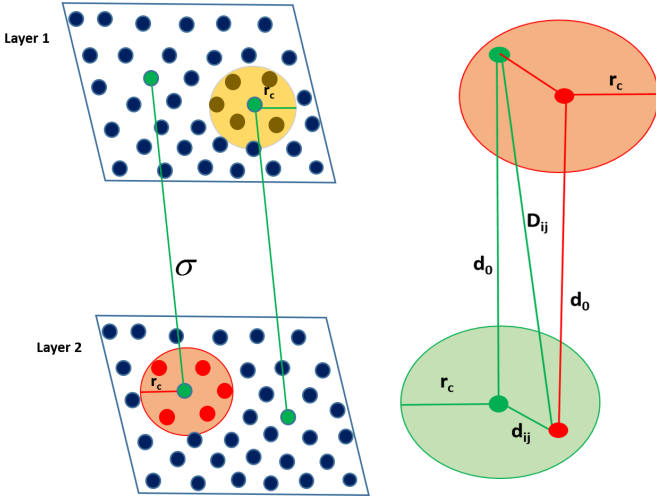
FIG. 1. Schematic representation of two coupled layers and their range interaction.

follows in the absence of interlayer coupling:

$$\dot{X}_i = v_i + \frac{1}{N} \sum_{j \neq i}^{N} \left\{ \frac{X_j - X_i}{|X_j - X_i|} [A + J \cos(\theta_j - \theta_i)] \right.$$

$$\left. - B \frac{X_j - X_i}{|X_j - X_i|^2} \right\}, \tag{3}$$

$$\dot{\theta}_i = w_i + \frac{K}{N} \sum_{j \neq i}^{N} \frac{\sin(\theta_j - \theta_i)}{|X_j - X_i|}. \tag{4}$$

In Eqs. (3) and (4), A and B are constant ($A = B = 1$), K is a constant which, multiplied by $1/|X_i - X_j|$, represents the coupling between the phases of the internal dynamics, and the interaction between the space and phase dynamics is modulated by the term $A + J \cos(\theta_j - \theta_i)$. Depending on the value of J, there can be attraction or repulsion between entities. For simplicity, we choose identical swarmalators $v_i = v$ and $\omega_i = \omega$, and therefore we take v and ω equal to zero without loss of generality.

Five main spatial configurations of entities are possible as a function of the pair (J, K), as presented in Ref. [14]. Many other patterns have been observed trying to show the effect of the coupling parameters on the aggregation and synchronization of swarmalators. Jiménez Morales has shown that this system can have a dynamically synchronized or asynchronous state and many others due to the form of the repulsive interaction term [70].

The effect of the phase coupling parameter was also observed in Refs. [44,69], where it was shown that the coupling disorder could lead to a synchronized state. Sar *et al.* [18] studied the competitive behavior between the positive and negative values of phase coupling. According to this description, the authors showed that we can have mixed patterns, clusters, and synchronization.

This study will consider two coupled layers of identical $N_1 = N_2 = N$ elements free to move in a two-dimensional space inside each layer. The interlayer coupling is assumed to be between an element of a layer with those elements in the other layer within the vision or interaction range, r_c, centered

at the projection of the coordinates of the first element on the second layer and vice versa, as described in Fig. 1.

To express the connection between the layers, let us define the new evolution of the state variable θ by introducing the interlayer coupling strength as follows:

$$\dot{\theta}_i^m = \underbrace{\frac{K_m}{N} \sum_{j \neq i}^{N} \frac{\sin(\theta_j^m - \theta_i^m)}{|X_{ij}^m - X_i^m|}}_{\text{intra layer dynamics}} + C_{\text{att}}^m(X_{ij}^m, \theta_{ij}^{ml}) + C_{\text{rep}}^m(X_{ij}^m, \theta_{ij}^{ml}),$$

$$\tag{5}$$

where $m = 1, 2$ identifies the layer, θ_i^m represents the internal phase of element i in layer m, $\theta_{ij}^{ml} = \theta_i^m - \theta_j^l$, and $X_{ij}^m = X_j^m - X_i^m$,

$$C_{\text{att}}^m = \underbrace{\frac{\sigma_a}{N_a^m} \sum_{j \neq i}^{N} F_a^l(i, j) \frac{\sin(\theta_j^l - \theta_i^m)}{D_{ij}^m}}_{\text{Attractive inter layer dynamics}}, \tag{6}$$

$$C_{\text{rep}}^m = \underbrace{\frac{\sigma_r}{N_r^m} \sum_{j \neq i}^{N} F_r^l(i, j) \frac{\sin(\theta_j^l - \theta_i^m)}{D_{ij}^m}}_{\text{Repulsive inter layer dynamics}}, \tag{7}$$

where $\sigma_a > 0$ and $\sigma_r < 0$ are the interlayer coupling strength for attractive and repulsive interaction respectively. N_a^m is the number of elements with attractive interaction inside the vision range in layer m and N_r^m those in the layer m which are not inside the vision range and therefore have a repulsive interaction. F_a^l and F_r^l are the $N \times N$ matrices representing the attractive and repulsive interlayer interaction, respectively. These functions show the connectivity (attractive or repulsive) created by the ith element with those in the opposite layer:

$$F_a^l(i, j) = \begin{cases} 1 & \text{if } j^{(l)} \in \Delta_{i_{(m)}}^{(l)}[r_c^{(l)}], \\ 0 & \text{otherwise} \end{cases}$$

$$F_r^l(i, j) = \begin{cases} 1 & \text{if } j^{(l)} \notin \Delta_{i_{(m)}}^{(l)}[r_c^{(l)}], \\ 0 & \text{otherwise} \end{cases} \tag{8}$$

where $l = (1, 2)$, $m = (1, 2)$, and $\Delta_{i_{(m)}}^{(l)}[r_c^{(l)}]$ is the set of elements inside the domain [vision range $r_c^{(l)}$] created around the projection of the ith element of layer m onto layer l. Indeed, for a chosen element in layer 1 (green one), the corresponding position in layer 2 (also green and not necessarily occupied by a swarmalator) is considered the center of a vision range of radius r_c. This vision range defines the space where the elements inside are connected through attractive coupling to a chosen one in layer 1. The swarmalators are globally connected inside each layer. We also assume that the Euclidean distance between swarmalators and the center of the vision range in the same layer is defined by d_{ij}^l, and this must be different from zero and less than some value, r_c, to avoid collision between entities.

The distance between the two layers is supposed to be a constant d_0. Therefore, the Euclidean distance between the ith element of layer 1 and the jth swarmalator in layer 2 is defined by D_{ij}^m [Eq. (9)],

$$D_{ij}^m = |X_j^m - X_i^l| = \sqrt{(d_{ij}^m)^2 + (d_0)^2}. \tag{9}$$

Therefore, according to the above description, the connection between the green element with the red elements (or the yellow one when analyzing the lower layer) inside the vision range is attractive [see Eq. (6)] and repulsive with those outside [see Eq. (7)]. This is to show the effect of connected elements on the whole dynamics of the layers when they are subject to a vision range interaction.

III. ORDER PARAMETERS

In order to investigate synchronization in our network, we define different types of order parameters to quantify the degree of intra- and interlayer phase synchronization. Besides that, we define the complex order parameter S [14–16,70] to find out the correlation between the phase and spatial dynamics.

The Kuramoto order parameter is defined as [71]

$$Re^{j\Phi} = \frac{1}{N} \sum_{i=1}^{N} e^{j\theta_i}, \tag{10}$$

where $j^2 = -1$ and Φ is the average of the phase of all elements in the network. However, when the ith and jth particles are synchronized, then the norm R tends to be 1. Then, if $R < 1$ (or near zero), then there is no phase synchronization.

To measure the correlation between the spatial angle ϕ and the internal phase dynamics θ of swarmalators, we define another order parameter S:

$$S_{\pm}e^{j\Psi_{\pm}} = \frac{1}{N} \sum_{i=1}^{N} e^{j(\phi_i \pm \theta_i)}, \tag{11}$$

with S being the maximum value between S_+ and S_-. Then, $S = \max(S_+, S_-)$ is the complex order parameter, and if $S = 1$, then there is full correlation between ϕ and θ of elements in the same layer, while if $S \approx 0$, then it indicates lack of correlation.

The following intra- and interlayer synchronization errors were used to analyze the phase synchronization inside each layer and between them, respectively. Let us define E_m and E_{ml}, the intra- and interlayer root mean square errors, as follows:

$$E_m = \sqrt{\frac{1}{N^2} \sum_{i,j}^{N} \left(\theta_i^m - \theta_j^m\right)^2}, \tag{12}$$

$$E_{ml} = \sqrt{\frac{1}{N^2} \sum_{i,j}^{N} \left(\theta_i^m - \theta_j^l\right)^2}. \tag{13}$$

In order to characterize the existence of static and active states, Eq. (14) defines the average velocity of elements in each layer,

$$V_m = \frac{1}{N} \sum_{i=1}^{N} v_i^m, \tag{14}$$

where $m = (1, 2)$ and $v_i^m = \sqrt{(\dot{x}_i^m)^2 + (\dot{y}_i^m)^2}$. However, when $V_m \approx 0$, the elements describe static (or quasistatic) dynamics, while for $V_m > 0$, the dynamics is active [69,72].

IV. NUMERICAL RESULTS

We consider a system of $N_1 = N_2 = N = 50$ identical swarmalators. For the numerical integration, Heun's method algorithm was used with a time step $dt = 0.05$, a transient time $t_{\min} = 90\%$ of the final time such that the last 10% correspond to 2×10^5 iterations. The spatial initial conditions were uniformly distributed between $[-1; 1]$, and the phase was distributed between $[-\pi; \pi]$. This section shows the dynamics of the layers (the case of layer 1 is presented here (see Fig. 2) while some results for the case of layer 2 are shown in Fig. 1 to 12 of the supplemental material [73]) when the vision range is applied and the mutual effect of the intra- and interlayer attractive and repulsive coupling force. To better analyze the effect of the attractive interlayer coupling σ_a, we have considered the case where the repulsive interaction between the two layers does not exist. This highlights the existence of a first-order-like phase transition to interlayer phase synchronization. Cluster, static synchronization and many other patterns have been observed which express the influence of the vision range r_c and that of the attractive and repulsive coupling strength between them.

A. Dynamics of two layers

The notions of attractive and repulsive interaction forces are essential in studying the evolution of swarmalators and are responsible for the aggregation phenomenon. They allow links between the different entities of the network to be created. In this study, the swarmalators in the layers are subject to an all-to-all attraction and repulsion. However, the interaction between an entity in one layer and those in the opposite layer is restricted by a vision range r_c (see Fig. 1). This interaction, as described by the equations of the above model [Eq. (5)], tells us about the nature of the interaction between the entity under consideration and those of the opposite layer.

1. Influence of vision range on static and active dynamics

In order to understand the influence of the vision range in the dynamics of a network with two layers, we recall that it depends on the set of parameters $(J, r_c, \sigma_a, \sigma_r)$, which are shown in Fig. 2, where the spatial and polar distribution of phases are represented. Varying them, the system passes through different active and passive dynamics states of synchronization and aggregation. Notice that the characterization of the dynamics states of the swarmalators [18] can be made based on the quantifiers grouped in Table I.

We can see in Fig. 3 a generalized evolution of these quantifiers (R, S, V) as a function of the vision range r_c for different values of the set (J, σ_a, σ_r) for the case of layer 1. We can observe in these evolutions the simultaneous effect of these three parameters on obtaining static or active intralayer dynamics of the swarmalators.

Indeed, for a weak value of the intralayer spatial coordininternal phase coupling strength $J = 0.1$ and for an attractive interlayer coupling strength lower than the repulsive interlayer coupling strength $(\sigma_a < |\sigma_r|)$, we can see that this leads to a transition from SA to SS without any intermediate states [see Fig 3(a)]. In fact, the phase synchronization is followed by the
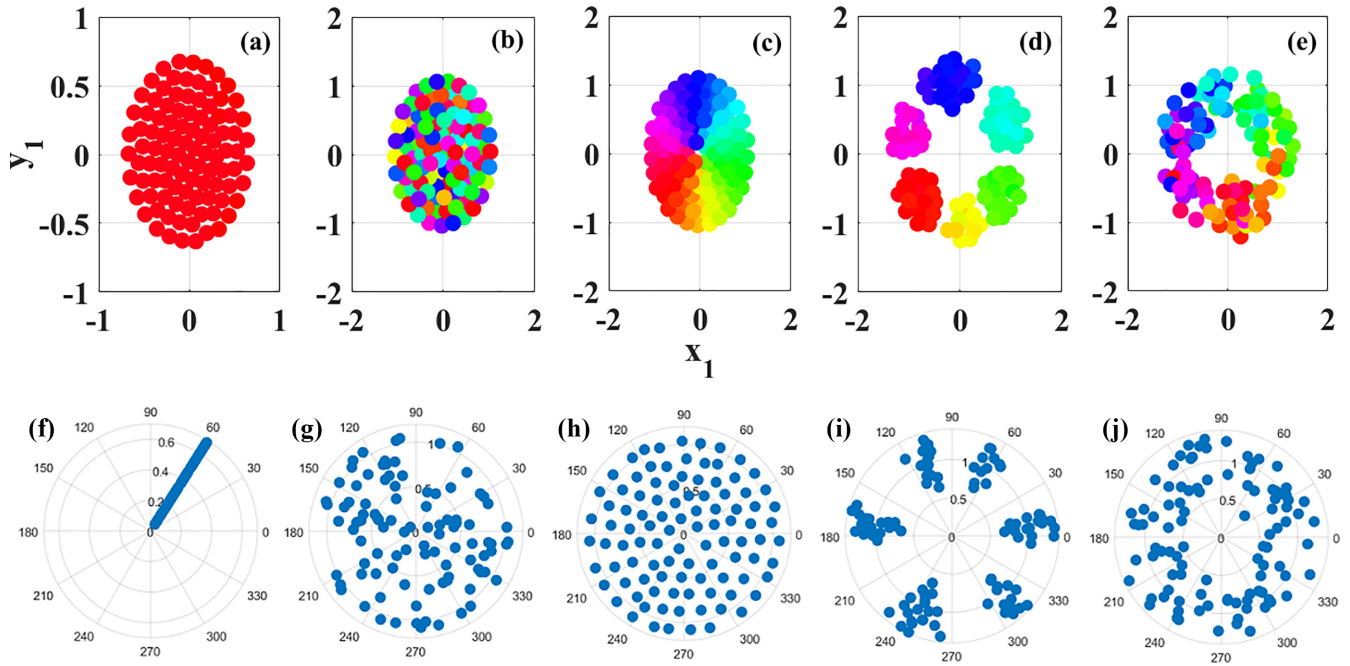
FIG. 2. Patterns formation of $N = 100$ swarmalators' dynamics according to Refs. [14,16] for chosen values of quadruplet $(J, r_c, \sigma_a, \sigma_r)$. The first row is the scatter plot in (X, Y) space, where the colors represent the value of the internal phase θ. The second row is the polar representation of the internal phase: [(a) and (f)] Static sync (SS) state for $(J, r_c, \sigma_a, \sigma_r) = (0.6, 2.55, 0.5, -0.5)$; [(b) and (g)] static async (SA) state for $(J, r_c, \sigma_a, \sigma_r) = (0.1, 2.5, 0.1, -1)$; [(c) and (h)] static phase wave (SPW) state for $(J, r_c, \sigma_a, \sigma_r) = (0.1, 0.5, 1, -0.1)$; [(d) and (i)] splintered phase wave (SpPW) state for $(J, r_c, \sigma_a, \sigma_r) = (0.6, 0.1, 0.1, -1)$; and [(e) and (j)] active phase wave (APW) state for $(J, r_c, \sigma_a, \sigma_r) = (0.99, 0.1, 0.5, -0.5)$. The intralayer phase coupling is $K_1 = K_2 = -0.1$ for the cases (a), (b), (c), and (d) and $K_1 = K_2 = -0.6$ for case (e), and the color indicates the phase θ (see Fig. 1 in the supplemental material for the case of layer 2 [73]).

formation of other states according to the following scheme:

$$SA \rightarrow SS \rightarrow AMPW \rightarrow SPW \rightarrow SA$$

$$r_c = 0.1 \rightarrow 0.65 \rightarrow 1.5 \rightarrow 1.65 \rightarrow \geqslant 2.$$

The scenario is similar for Figs. 3(b) and and 3(c) with the difference that the increase of the phase coupling strength J (for $J = 0.6$ and $J = 0.99$) and the prevalence of the interlayer repulsive coupling over the interlayer attractive coupling strength ($|\sigma_r| > \sigma_a$) favors the correlation between the inter-
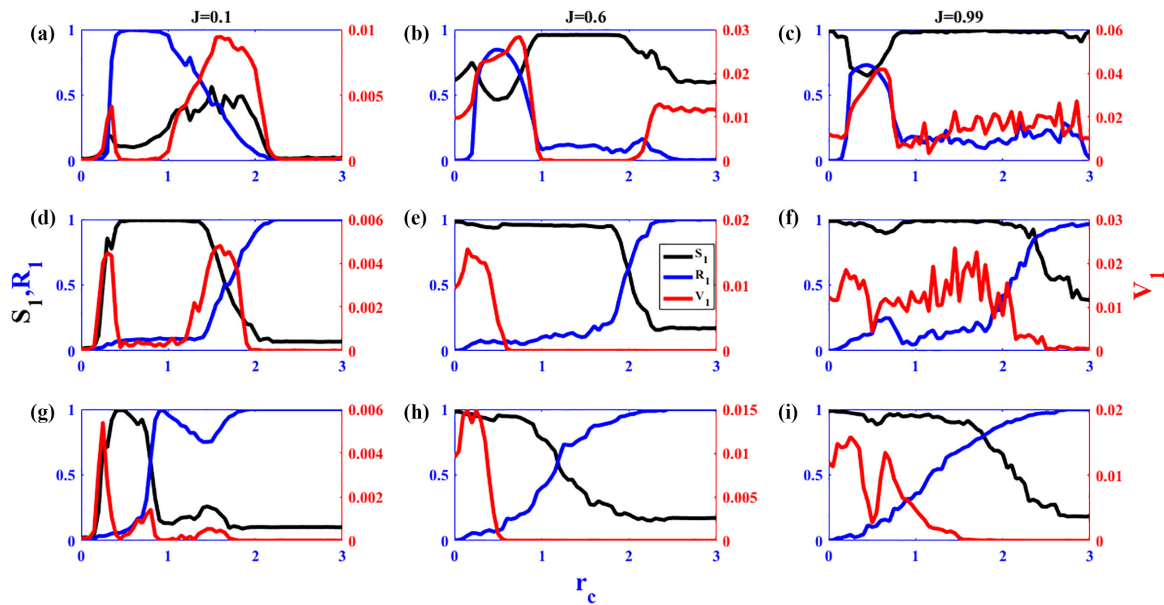

FIG. 3. Order parameters R (blue), correlation S (black) in the right axis, and mean velocity V (red) in the left axis as a function of vision range r_c for different values of triplet (J, σ_a, σ_r). The first row is for $(\sigma_a, \sigma_r) = (0.1, -1)$, the second one corresponds to $(\sigma_a, \sigma_r) = (0.5, -0.5)$, and the last row to $(\sigma_a, \sigma_r) = (1, -0.1)$ with $K_1 = K_2 = -0.1$ (see Fig. 2 in the supplemental material for the case of Layer 2 [73]).

TABLE I. Emerging patterns with order parameters R, S, and V used to quantify the states.

R	S	V	Patterns states
≈ 1	$0 < S < 1$	$\simeq 0$	Static sync (SS)
0	0	0	Static async (SA)
0	$\neq 0 (\approx 1)$	0	Static phase wave (SPW)
0	≈ 1	$\neq 0$	Splintered phase wave (SpPW) or Repulsive mixed phase wave (RMPW)
0	$\neq 0 (<1)$	$\neq 0$	Active phase wave (APW)
$\neq 0 (<1)$	$\neq 0$	≈ 0	Static π (SPI)
$\neq 0 (<1)$	≈ 1	≈ 0	Static cluster sync (SCS)
$\neq 0$	$\neq 0$	$\neq 0$	Attractive mixed Phase wave (AMPW)

nal and spatial phase S and disfavors this time the apparition of intra- and interlayer phase synchronization $R < 0.95$; we can remark here the absence of both intra- and interlayer phase synchronization. Nevertheless, in these figures the following transitions are observed:

$$\text{SpPW} \rightarrow \text{RMPW} \rightarrow \text{SPI} \rightarrow \text{SpPW}$$

$$r_c = 0.1 \rightarrow 0.25 \rightarrow 1.65 \rightarrow \geqslant 2.$$

Considering the complementary effect of the attractive and repulsive interlayer coupling strengths such as $(|\sigma_r| = \sigma_a)$, we can see in Figs. 3(d) and 3(e) a clear progressive transition towards intra- and interlayer phase synchronization, while although not so clearly it also appears in Fig. 3(f). Here phase synchronization is obtained when the vision range increases, whatever the value of the spatial coupling J is taken between 0 and 1.

For a small value of the phase coupling $J = 0.1$, even though the attractive and repulsive interlayer coupling strength are identical, there is a progressive transition to phase synchronization as shown in the following diagram:

$$\text{SA} \rightarrow \text{APW} \rightarrow \text{SPW} \rightarrow \text{AMPW} \rightarrow \text{SS}$$

$$r_c = 0.05 \rightarrow 0.3 \rightarrow 0.8 \rightarrow 1.7 \rightarrow \geqslant 2.$$

When J increases ($J = 0.6$ and $J = 0.99$), static clusters are formed. For low values of the vision range ($r_c = 0.1$), we have the formation of the SpPW [Figs. 3(e) and 3(f)]. For an increase of this radius ($r = 1.8$), the number of clusters tends to decrease, giving way to the formation of the SPI (with 2 clusters) followed by the SS. We note here the weak presence of an active state due to the almost null variation of the average velocity when $0.5 < r_c < 1.2$ and $r_c > 2$ [Fig. 3(d)]. However, when $J = 0.6$ [Fig. 3(e)], we observe a correlation between the spatial phase ϕ and the internal phase θ for $r_c < 2$. This persistence of the correlated state between the phases here reflects the existence of SpPW states for $r_c < 0.5$ followed by the SPI when $0.5 < r_c < 2$ [Fig. 3(e)], the transition scheme to static phase synchronization in Fig. 3(e) is as follows:

$$\text{SpPW} \rightarrow \text{SPI} \rightarrow \text{SS}$$

$$r_c < 0.5 \rightarrow 0.5 < r_c < 2 \rightarrow r_c \geqslant 2.$$

In Fig. 3(f), the SpPW is, however, followed by the formation of the SCS [18] (see Fig. 3 and video 1 in the supplemental material the snapshot of SCS state [73]) at $r_c = 0.5$ before reaching the SPI and SS. This state appears for the triplet $R \neq 0 (< 1)$, $S \approx 1$, and $V \approx 0$,

$$\text{SpPW} \rightarrow \text{SCS} \rightarrow \text{SPI} \rightarrow \text{SS}$$

$$r_c < 0.5 \rightarrow r_c = 0.5 \rightarrow 0.5 < r_c < 2 \rightarrow r_c \geqslant 2.$$

However, considering that the repulsive coupling is such that $|\sigma_r| < \sigma_a$, we obtain the evolutions of Figs. 3(g), 3(h) and 3(i). From these evolutions, the synchronization is as quickly reached as in the case of Figs. 3(d), 3(e) and 3(f). Nevertheless, we can see that when the spatial coupling J increases ($J = 0.99$), the synchronization region decreases. Indeed, for $J = 0.1$ [Fig. 3(g)], we observe a synchronization state when $r_c \geqslant 1.65$. This state is preceded by the formation of MPW, SPW, and SA:

$$\text{SA} \rightarrow \text{RMPW} \rightarrow \text{SPW} \rightarrow \text{AMPW} \rightarrow \text{SS}$$

$$r_c \leqslant 0.1 \rightarrow 0.25 \rightarrow 0.5 \rightarrow 1.45 \rightarrow r_c \geqslant 1.65.$$

In Fig. 3(h), we observe an absence of SPW and MPW when $J = 0.6$ and a slight reduction of the synchronization width ($r_c \geqslant 2$). The transition to synchronization is as follows:

$$\text{SpPW} \rightarrow \text{SPI} \rightarrow \text{SS}$$

$$r_c \leqslant 0.3 \rightarrow 0.95 \rightarrow r_c \geqslant 2.$$

In contrast to Figs. 3(g) and 3(h), in Fig. 3(i), $J = 0.99$ does not favor static states' formation when $r_c \leqslant 2.5$. Nevertheless, we have the formation of SPI states when $r_c = 1.5$, and of SCS $r_c = 0.6$ and synchronization appears when $r_c \geqslant 2.55$. These states are preceded by the SpPW for $r_c < 0.3$,

$$\text{SpPW} \rightarrow \text{SCS} \rightarrow \text{SPI} \rightarrow \text{SS}$$

$$r_c \leqslant 0.3 \rightarrow 0.6 \rightarrow 1.5 \rightarrow r_c \geqslant 2.55.$$

In addition to the states described earlier, we noticed that the transition observed in Figs. 3(d) and 3(g) pass through a formation in space of an attractive dynamics with $R \neq 0$, $S < 1$, $V > 0$ and respectively for $r_c = 1.7$ and $r_c = 1.45$, while the formation of clusters passes through a repulsive dynamics with $R = 0$, $S \approx 1$, $V > 0$ [Figs. 3(b), 3(c) and 3(g)] with $r_c = 0.25$. These states were called a *mixed phase wave* corresponding to an attractive (AMPW) and repulsive (RMPW) [18].

Note that in Fig. 3(a), the phase synchronization obtained when $0.4 < r < 1$ is intralayer and not interlayer. To better appreciate the synchronous behavior of Fig. 3, we have plotted in Figs. 4 the evolution of the interlayer phase difference as well as the intralayer (E_1 and E_2) and interlayer (E_{12}) synchronization errors as a function of the vision range for some values of spatial coupling strength J and the interlayers coupling strengths (σ_a, σ_r).

From all the data shown in these figures, we notice that the transition to intralayer synchronization and interlayer occurs for the vision range $r_c \geqslant 2$. However, the weakly value of the spatial coupling J is not advantageous to lead the systems to interlayer phase synchronization. That is why in Fig. 4(c) we do not have a zero value of the interlayer error ($E_{12} \neq 0$),
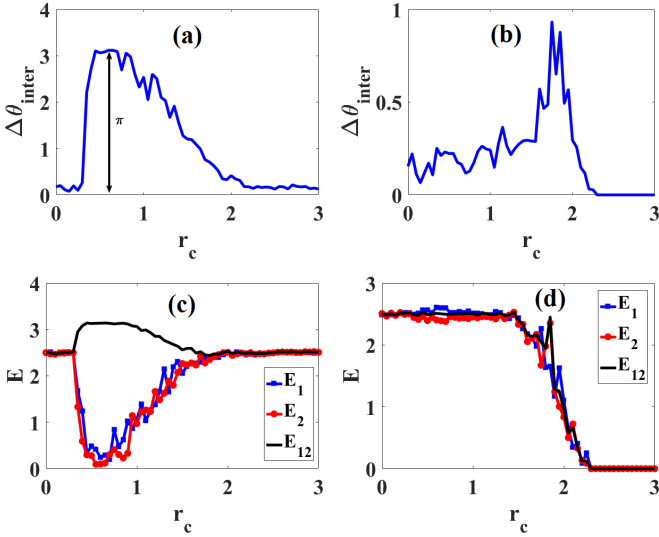
FIG. 4. Evolution of the interlayer phase difference [(a) and (b)] and mean error [(c) and (d)] as a function of the vision range r_c for chosen values of spatial phase coupling strength J. E_1 and E_2 are respectively the intralayers errors of L1 and L2, E_{12} is the interlayer error of synchronization. This was plotted for [(a) and (c)] $J = 0.1$, $\sigma_a = 0.1$, $\sigma_r = -1$ and in [(b) and (d)] $J = 0.1$, $\sigma_a = 0.5$, $\sigma_r = -0.5$ with $K_1 = K_2 = -0.1$.

but we only have phase synchronization ($E_1 \approx 0$ and $E_2 \approx 0$) inside each layer for a small region $r_c < 1$. This result implies that the existence of intralayer phase synchronization is not a sufficient condition to achieve interlayer phase synchronization. However, it is essential to have it. This achievement of phase synchronization also depends on the chosen values of systems parameters like the intra- and interlayers coupling strengths. According to Figs 4(a) and 4(c), both systems are intralayer synchronized when $J = 0.1$ and $\sigma_a < |\sigma_r|$ when $0.4 < r_c < 1$ and antisynchronized between different layers.

2. Interlayer static sync PI (ISSPI)

As we just saw, depending on the mutual influence of the layers, there is no interlayer phase synchronization, but it exists an interlayer antiphase synchronization [Figs 5(a) and 5(b)] which can be seen in Figs. 4(a) and 4(c). The antiphase synchronization in swarmalators was described in Ref. [18] as a SPI state if this appears with a small spatial displacement of elements for a system with a single layer. Since this work
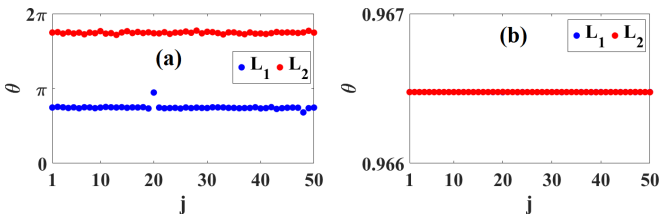

FIG. 5. Snapshot of the the phase of swarmalators for different values of J: (a) antiphase synchronization between L1 and L2 for $(J, r_c, \sigma_a, \sigma_r) = (0.1, 0.65, 0.1, -1)$ and (b) phase synchronization between L1 and L2 for $(J, r_c, \sigma_a, \sigma_r) = (0.6, 2.5, 0.5, -0.5)$.
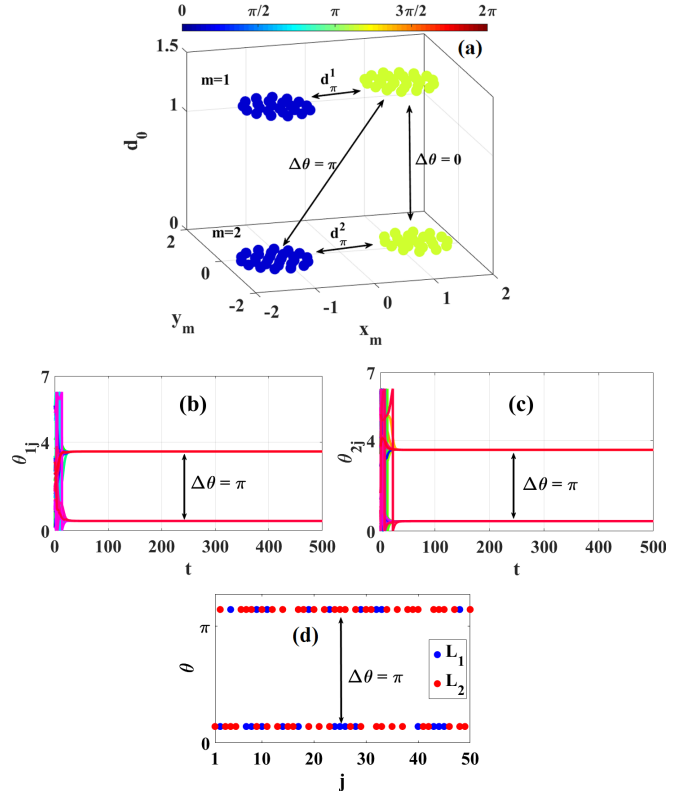

FIG. 6. ISSPI dynamics. (a) Scatter plot showing the ISSPI dynamics with the distance (d_0) between layers; (b) time evolution of phase of entities on layer 1; (c) time evolution of phase of entities on layer 2; and (d) phase distribution of nodes in the two layers, with red for layer 2 and blue for layer 1. This was plotted for $J_1 = J_2 = 0.6$, $r_c = 1.5$, $\sigma_a = 0.1$, $\sigma_r = -1$, and $K_1 = K_2 = -0.1$ (see video 2 in the supplemental material [73]).

treats the case of two mutually interacting layers, we call this effect the *interlayer static sync π (ISSPI) state* [see Fig. 6(a)].

We are now going to consider a configuration where elements inside each layer formed two clusters that are independently static and synchronous, with a phase difference between them equal to π (intrastatic π) and also a phase difference equal to π with those of the opposite layer showing an interlayers antiphase synchronization (see Fig. 6).

To summarize, the ISSPI state is described by the following properties:

(i) P_1: There is a *static PI* state inside each layer. This means we have the formation of two clusters inside each layer with a phase difference equal to π between them [Figs. 6(b) and 6(c)].

(ii) P_2: A cluster in layer 1 synchronizes with a cluster in layer two which is formed by the set of swarmalators at a distance r_c centered at the projection of a given element in the cluster in layer 1 and the same for a cluster on layer 2 [Fig. 6(d)].

(iii) P_3: The phase difference between the lower clusters of layer 1 and the upper one of layer 2 is equal to π [Fig. 6(d)].

These three properties allow us to describe the ISSPI state, which is observed in Fig. 6, where we have a formation of two static clusters (C_1 and C_2) inside each layer, as shown by the evolution of the internal phase of the swarmalators. We

can see the phase difference $\Delta\theta = \pi$ between the opposite clusters of each layer.

3. Stability analysis of ISSPI

According to the first property, P_1, let $\bar{X}_i^m$ be the center of mass of each cluster inside layer m and ς_i the number of elements in the set of swarmalators inside the ith cluster of layer m. Then we can write

$$\bar{X}_i^m = \frac{1}{\varsigma_i} \sum_{j \in \varsigma_i} X_j^m \quad (i = 1; 2). \tag{15}$$

When the synchronized clusters appear in both layers, we can apply the properties P_2 and P_3,

$$\text{int}er \begin{cases} \theta_1^1 = \theta_1^2 \\ \theta_2^1 = \theta_2^2 \end{cases} \quad \text{int}ra \begin{cases} \theta_1^1 \neq \theta_2^1 \\ \theta_1^2 \neq \theta_2^2 \end{cases}. \tag{16}$$

Using Eq. (4) for each cluster on each layer, we have

$$\dot{\bar{X}}_i^m = \frac{1}{N} \left\{ \frac{\bar{X}_j^m - \bar{X}_i^m}{|\bar{X}_j^m - \bar{X}_i^m|} \left[1 + J_m \cos\left(\theta_j^m - \theta_i^m\right)\right] - \frac{\bar{X}_j^m - \bar{X}_i^m}{|\bar{X}_j^m - \bar{X}_i^m|^2} \right\}$$

$$\dot{\theta}_i^m = \frac{K_m}{N} \left[\frac{\sin\left(\theta_j^m - \theta_i^m\right)}{|\bar{X}_j^m - \bar{X}_i^m|}\right] + \frac{\sigma_a}{N_a^m} \frac{\sin\left(\theta_i^l - \theta_i^m\right)}{D_{12}^m}$$

$$+ \frac{\sigma_r}{N_r^m} \frac{\sin\left(\theta_i^l - \theta_i^m\right)}{D_{12}^m} \quad i \neq j \text{ and } l \neq m. \tag{17}$$

Let us use d_{ij}^l, defined in Sec. II: $d_{ij}^l = |\bar{X}_i^l - \bar{X}_j^l| \; i \neq j, \; (l = 1; 2)$, then

$$\text{static state} \Rightarrow \begin{cases} \dot{\bar{X}}_1^1 = 0 \\ \dot{\bar{X}}_1^2 = 0 \end{cases}, \tag{18}$$

and, therefore,

$$d_{ij}^l = \frac{1}{1 + J_l \cos\left(\theta_i^l - \theta_j^l\right)}. \tag{19}$$

Using Eq. (16), we can say that the maximum spatial distance between the two clusters inside a lth layer (without interaction with another layer) is lower or equal to d_π^l, where d_π^l is the value of d_{ij}^l for $(\theta_i^l - \theta_j^l) = \pi$ [18]:

$$d_\pi^l = \frac{1}{(1 - J_l)}. \tag{20}$$

It means that the minimum value of vision range r_c where static synchronization appears inside each layer is such as $r_c \geqslant \frac{1}{(1-J_l)}$ (also without interaction with another layer). This was demonstrated as a necessary condition for synchronization inside each layer [18]. Now, due to the interaction between the two layers, we showed that the relation between the maximum distance of the cluster inside each layer is given by

$$d_\pi^m = \frac{1 - J_l}{1 - J_m} d_\pi^l \quad (m, l = 1; 2). \tag{21}$$

In this case, we can simply express the minimal vision range $r_c \geqslant \frac{1}{(1-J)}$. This evolution shows us the second-order

transition to phase synchronization inside each layer and between the two layers, as shown in Figs. 3 and 4. However, to analyze the stability of ISSPI, we define the error of synchronization ε_i between the ith clusters in different layers as follows:

$$\varepsilon_i = \theta_i^2 - \theta_i^1 \quad (i = 1; 2). \tag{22}$$

Then its time derivative is

$$\dot{\varepsilon}_i = \dot{\theta}_i^2 - \dot{\theta}_i^1. \tag{23}$$

Let us take $\Delta\theta^m = \theta_2^m - \theta_1^m \; (m = 1,2)$, the phase difference between the two clusters in layer m.

Using Eq. (5) in the ISSPI, where the number of clusters is $N = 2$ (in the two layers) with $N_a^1 = N_a^2 = 1$ and $N_r^1 = N_r^2 = 1$, the time derivative of the error becomes

$$\dot{\varepsilon}_i = g(\theta) + (\sigma_a + \sigma_r)\frac{\sin\left(\theta_i^1 - \theta_i^2\right)}{D_{12}^2}$$

$$- (\sigma_a + \sigma_r)\frac{\sin\left(\theta_i^2 - \theta_i^1\right)}{D_{12}^1}, \tag{24}$$

with $g(\theta) = \frac{K_2}{2}\left[\frac{\sin(\Delta\theta^2)}{d_\pi^2}\right] - \frac{K_1}{2}\left[\frac{\sin(\Delta\theta^1)}{d_\pi^1}\right]$.
For $\theta_i^2 - \theta_i^1$ near zero, we can write

$$\dot{\varepsilon}_i = g(\theta) + (\sigma_a + \sigma_r)\frac{(-\varepsilon_i)}{D_{12}^2} - (\sigma_a + \sigma_r)\frac{\varepsilon_i}{D_{12}^1}. \tag{25}$$

Knowing that one of the conditions to have ISSPI state is first having a static PI state inside each layer. This means $\Delta\theta^1 = \Delta\theta^2 = k\pi \; (k \in \mathbb{Z}) \Rightarrow g(\theta) = 0$.
The Eq. (25) becomes

$$\dot{\varepsilon}_i = (-\varepsilon_i)(\sigma_a + \sigma_r)\left(\frac{1}{D_{12}^2} + \frac{1}{D_{12}^1}\right), \tag{26}$$

the solution of Eq. (26) is expressed as

$$\varepsilon_i(t) = \exp\left\{-\int (\sigma_a + \sigma_r)f(r_c)\, dt\right\}, \tag{27}$$

where

$$f(r_c) = \left(\frac{1}{D_{12}^2} + \frac{1}{D_{21}^1}\right)$$

and D_{12}^m is defined by Eq. (9). The expression of the solution of Eq. (27) shows that, since $f(r_c) > 0$, the ISSPI is always stable if $\sigma_a + \sigma_r \geqslant 0$ and the error, $\varepsilon_i(t)$, between both layers converges to zero as long as $\int (\sigma_a + \sigma_r)f(r_c)\, dt$ is large. However, in the case $\Delta\theta^1 = \Delta\theta^2 \neq k\pi \Rightarrow g(\theta) = G \neq 0$ and $f(r_c) = f > 0$, the error defined by Eq. (25) can be rewritten:

$$\dot{\varepsilon}_1 = G - \varepsilon_1(\sigma_a + \sigma_r)f(r_c). \tag{28}$$

The generalized Lyapunov function can be defined by the quadratic form of the error as

$$Q = \sum_i Q_i \quad (i = 1; 2), \tag{29}$$

with

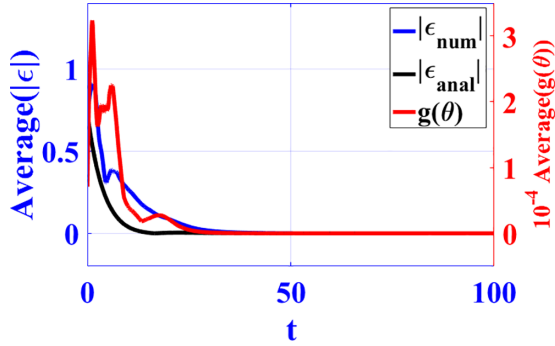$$Q_i = \frac{1}{2}(\varepsilon_i)^2. \tag{30}$$

FIG. 7. Convergence of the mean error. $|\varepsilon_{\text{anal}}|$ and $|\varepsilon_{\text{num}}|$ are respectively the analytical error (in blue) which is the solution of the Eq. (26) and numerical error (in black) described by Eq. (22); the red curve is the function $g(\theta)$ describes in Eq. (24). This was plotted in the ISSPI conditions with $J = 0.6$, $K_1 = K_2 = -0.1$, $\sigma_a = 0.1$, $\sigma_r = -1$, $r_c = 1.5$.

The time derivative of Lyapunov function is given by

$$\dot{Q}_i = \dot{\varepsilon}_i.\epsilon_i = \varepsilon_i.G \, - \, (\varepsilon_i)^2(\sigma_a + \sigma_r)f(r_c),$$
$$\dot{Q}_i \leqslant |\varepsilon_i||G| \, - \, (\varepsilon_i)^2(\sigma_a + \sigma_r)f(r_c), \qquad (31)$$

for $\sigma_a + \sigma_r \neq 0$, we can write

$$\dot{Q}_i \leqslant - (\sigma_a + \sigma_r)f\left[|\varepsilon_i| - \frac{|G|}{2(\sigma_a + \sigma_r)f(r_c)}\right]^2$$
$$+ \frac{G^2}{4(\sigma_a + \sigma_r)f(r_c)}.$$

For $\sigma_a + \sigma_r \geqslant 0$, the time derivative of the Lyapunov function becomes

$$\dot{Q}_i \leqslant G_M, \qquad (32)$$

where $G_M = \max[\frac{G^2}{4(\sigma_a+\sigma_r)f(r_c)}]$.

It is established that the system defined by Eq. (28) is practically stable [7,74] since the time derivative of the Lyapunov function in Eq. (32) is bounded by a positive constant. According to Sekieta and Kapitaniak [75] and Fermat and Solis-Perales [76], in practical synchronization, the error dynamics is not converging to zero but to a sufficiently small value that can be considered as the tolerance domain of the synchronization condition. The results for our system are shown in Fig. 7.

B. Influence of repulsive interaction (σ_r)

The interaction between the elements of the different layers highlights the attractive and repulsive forces as described in Eqs. (1) and (5). This is done through the intra- and interlayer attractive and repulsive coupling forces (σ_a, σ_r). As shown previously, the attractive interaction allowed us to highlight the existence of an intra- and interlayer phase synchronization by keeping constant the repulsive coupling force σ_r. However, we found that for specific values of the repulsive coupling force (by fixing the attractive coupling σ_a), the state of phase synchronization could no longer be reached, leaving room for desynchronization. Although reflecting the repulsion between the entities out of the vision range and the considered element

of the opposite layer, the variation of the interlayer repulsive coupling lets us perceive the formation of static and active state dynamics of the swarmalators in layer 1. As described above, the transition to synchronization in some cases passes through the formation of intermediate state that clearly highlights the effect of attractive and repulsive coupling called the mixed phase wave (MPW) shown in Fig. 8. Indeed, we notice in Fig. 9 the formation of active states (SpPW and APW, in red) and static states (SS in blue and SA and SPW in white).

It can be seen that increasing the repulsive coupling favors the formation of active states while decreasing it favors the formation of static states. This characterizes the fact that the continued existence of repulsion between the elements of the network creates a permanent agitation between them. The opposite process is observed as the vision range and the interlayer repulsive coupling strength σ_r decrease.

In addition to the formation of static and active states, the evolution of Fig. 10 highlights that the transition from phase synchronization to an asynchronous state when the repulsive coupling force σ_r decreases is of the first order. Thus, we can notice two evolutions on the Fig. 10, one in blue highlighting an evolution of the order parameters for a value of $\sigma_a = 1.5$ and red corresponding to a value of $\sigma_a = 2$. From this evolution, we can see that the increase of the attractive coupling σ_a increases the inter- and intralayer phase synchronization area [Fig. 10(a)]. However, this increase in repulsive coupling favors the correlation [Fig. 10(b)] between the spatial phase ϕ and the internal phase (θ) in both layers for a threshold $S_m \geqslant 0.97$ $(m = 1, 2)$ when $|\sigma_r| \geqslant 0.5$. A detailed study shows that these transitions depend on the initial conditions, as can be seen in Fig. 10 and Figs. 5–7 of the supplemental material [73]). A thorough study of the regions of parameters where explosive transitions occur is beyond the scope of this work.

Figures 11 shows the mutual influence of the interlayer repulsive coupling σ_r and the vision range r_c on the inter- and intralayer evolution toward the phase synchronization state. For a growing repulsive coupling evolution, we observe an intralayer decoherence state (blue) for R_1 less than 0.95 [see Fig. 11(a)] and an interlayer one characterized by an interlayer error $E_{12} \neq 0$ [Fig. 11(b)] when the vision range is low ($r_c \leqslant 2$). On the other hand, the decrease of the coupling σ_r expressing the progressive absence of agitation in the system favors this time a first-order transition (when $\sigma_r \leqslant 0.25$) towards the state of phase synchronization (cyan) intralayer shown by $R_1 \simeq 1$ and interlayer ($E_{12} \approx 0$) [Figs. 11(a) and 11(b)]. This transition towards synchronization suggests the progressive dominance of the attractive interlayer interaction forces over the repulsive ones as the vision range r_c increases.

C. Influence of attractive interaction (σ_a)

In contrast to the repulsive interlayer coupling σ_r, increasing the attractive interlayer coupling σ_a favors not only the formation of static states but also the convergence of the system elements towards a state of phase synchronization, as can be seen in Fig. 12, where the formation of static states is represented in blue and active ones in red.
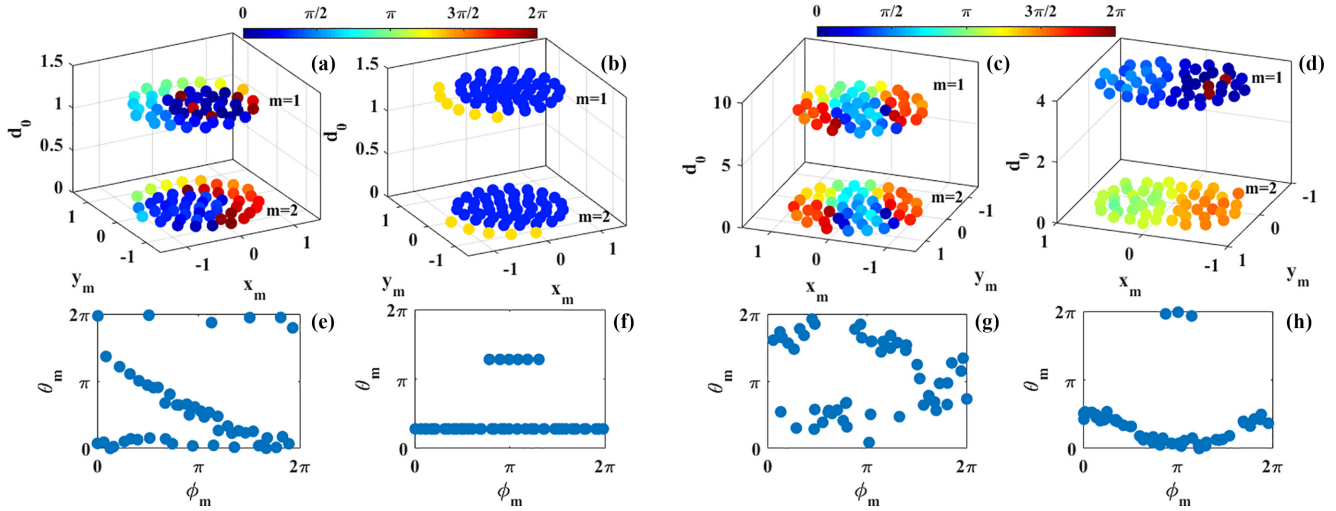
FIG. 8. Mixed phase wave state under the influence of quadruplet $(J, r_c, \sigma_a, \sigma_r)$ in the two layers with the corresponding (θ, ϕ) space. AMPW appears with $J = 0.1$ for [(a) and (e)] $\sigma_a = 0.5$, $\sigma_r = -0.5$, $r_c = 1.7$ and [(b) and (f)] $\sigma_a = 1$, $\sigma_r = -0.1$, $r_c = 1.45$. RMPW appears for [(c) and (g)] $J = 0.1$, $\sigma_a = 1$, $\sigma_r = -0.1$, $r_c = 0.25$, and [(d) and (h)] $J = 0.6$, $\sigma_a = 0.1$, $\sigma_r = -1$, $r_c = 0.25$. The color represents the internal phase θ.

This influence of the attractive coupling is also observed in intra- and interlayer synchronization dynamics, as seen in the evolution of Fig. 13, the phase synchronization (cyan) and decoherence (blue).

It should be noted that the synchronous behavior obtained is intra- and interlayer. For $R_1 \simeq 1$ and/or $R_2 \simeq 1$, we obtain intralayer synchronization when the vision range $r_c \geqslant 2$ and $\sigma_a \geqslant 0.2$ [Fig. 13(a)]. To verify the existence of interlayer synchronization, Fig. 13(b) shows the variation of the interlayer synchronization error E_{12}.
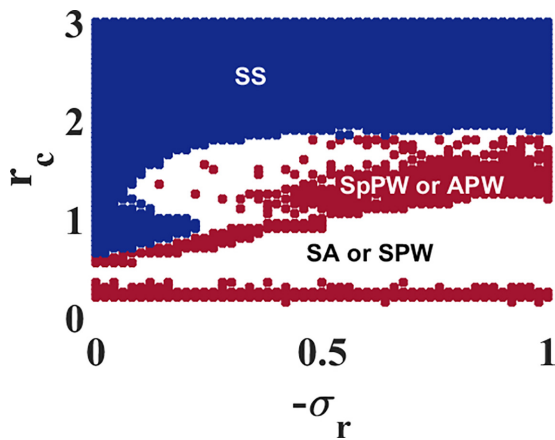
D. Absence of repulsive coupling: First-order transition

The simultaneous presence of attractive and repulsive couplings reveals second-order transitions to inter- and intralayer phase synchronization (see Fig. 3). However, to understand these transitions, we cancel the repulsive coupling, namely $\sigma_r = 0$, and only the attractive interaction is active ($\sigma_a \neq 0$). Thus varying σ_a the entire system presents a first-order transition to phase synchronization, as shown in Fig. 14. The graphs in Fig. 14 show the evolution of the order parameter and correlation for the first layer [Figs. 14(a) and 14(b)] for different values of r_c such as $r_c = 0.75$, $r_c = 1$, and $r_c = 3$. Comparing these curves, we conclude that (i) the first-order transition is obtained for large-enough values of r_c and (ii) for small values of r_c there is a high correlation between the spatial phases, ϕ_i [Eq. (11)], and the internal phase θ_i for each ith node, namely $S_1 = 1$, for an interval of values of σ_a that increases while r_c decreases. Here the coupled layers will achieve a second-order transition to phase synchronization as the probability of having nodes with whom interact attractively becomes very low since the interaction surface, defined
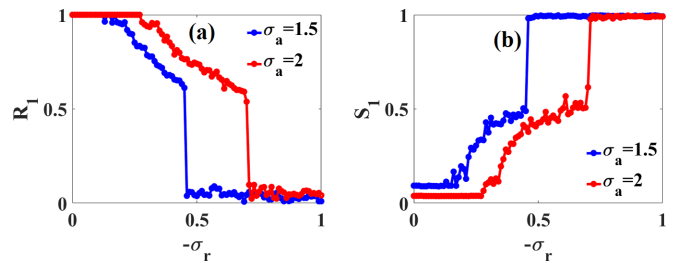

FIG. 9. Influence of repulsive coupling σ_r and vision range r_c on the active and static dynamics on layer 1. Red shows the active states: SpPW, APW, and the the static states: SS in blue and SPW and SA in white. This was plotted using the mean velocity for static state $V_m \approx 0$ and active $V_m > 0$. The intralayer phase coupling is chosen $K_1 = K_2 = -0.1$ and the spatial one $J_1 = J_2 = 0.1$ with $\sigma_a = 1.5$ (see Fig. 4 in the supplemental material for the case of layer 2 [73]).

FIG. 10. Effect of the repulsive coupling strength σ_r on the transition to intralayer phase synchronization for a particular initial condition. (a) Order parameter R_1 and (b) correlation S_1 of layer 1; as a function of the repulsive coupling σ_r for different values of the attractive coupling. Red is for $\sigma_a = 2$ and blue for $\sigma_a = 1.5$. This was plotted for $J_1 = J_2 = 0.1$, $K_1 = K_2 = -0.1$ and $r_c = 1$.
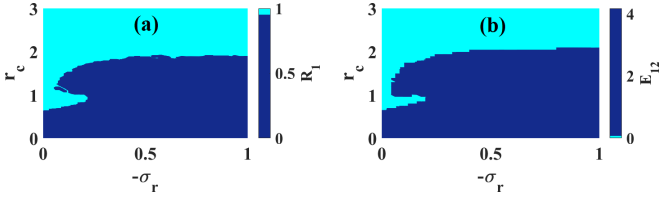
FIG. 11. Mutual influence of couple (σ_r, r_c) on each layer. (a) Order parameter R_1 of layer 1; (b) interlayer error of synchronization E_{12}. Cyan shows the synchronous state and the blue one the asynchronous state. The intralayer phase coupling is $K_1 = K_2 = -0.1$ and the spatial one $J_1 = J_2 = 0.1$ with $\sigma_a = 1.5$ (see Fig. 8 in then supplemental material for the case of layer 2 [73]).

by the circle with radius r_c, decreases (see Fig. 1). Also, the antagonist movements of R_1 that increase while S_1 decreases in all the considered cases coupled to the relation given by Eq. (11) show that each θ_i synchronizes only with its ϕ_i. At the same time, there is no synchronization between the θ_i as $R_i < 1$ in those cases.

Using the Hamiltonian formalism as given by Eq. (33),

$$H_i^m = -\frac{K_m}{2N_m} \sum_{j \neq i}^{N_m} \cos\left(\theta_j^m - \theta_i^m\right), \quad (m = 1; 2), \quad (33)$$

based on the mean-field XY model [72,77,78], we can see that the internal phase dynamics, independent of the layer, undergoes a series of transitions before stabilizing at synchronization, as seen in Fig. 15. These figures show the energy for both layers for $r_c = 0.75$, $r_c = 1$, and $r_c = 3$. For the latter, the system undergoes an explosive-type synchronization at $\sigma_a \approx 0.2$. When $0.09 \leqslant \sigma_a \leqslant 0.33$ for $r_c = 1$ and $0.09 \leqslant \sigma_a \leqslant 0.63$ for $r_c = 0.75$, there appear two significant transitions: (i) for r_c equal to 0.75 and 1, a drop, down from $H_i^m \simeq 0.037$ to $H_i^m \simeq 0.0362$ with $i = 1, 2$, and (ii) a jump, up to $H_i^m \simeq 0.039$ with $m = 1, 2$ to an apparent static complete synchronization, for $r_c = 3$. All cases show complete synchronization for $\sigma_a > 0.09$. Finally, we may notice that the range of the parameter σ_a between the two transitions increases while r_c decreases. This is due to the fact that the probability of connecting strongly
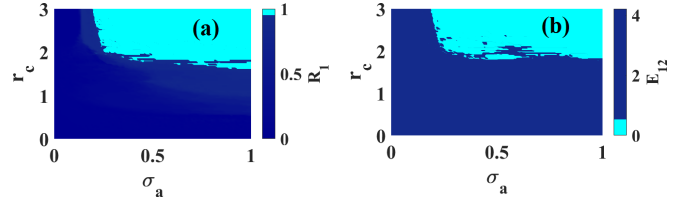
depends on the vision range, and it takes stronger attraction to synchronize when the range of attraction is smaller.

For a better understanding of the behavior of the energy H_i^m for the first and second layers, let us concentrate on the case $r_c = 0.75$ and compare it to that of $r_c = 3$ as shown by the mean velocity of each case [Figs. 15(c) and 15(d)].

The graphs in Figs. 15(c) and 15(d) are divided into different sections as a function of σ_a: (A1) and (B1), where the coherence instability is shown by the variation of the mean speed shown in Figs. 15(c) and 15(d). We recall that this is the region of Fig. 14(a) for which R_1 and S_1 are almost zero, meaning there is no synchronization on theta and no correlation between θ_i and ϕ_i. Increasing σ_a, we encounter (A2) and (B2) where augmenting the value of the attractive coupling strength increases the speed of the nodes in each network with different and opposite consequences, as can be seen by the behaviors of the energy, depending on the value of the vision range: For $r_c = 0.75$, the energy function H_1 just dropped, while in Fig. 15(d) for $r_c = 3$, it suddenly jumps to its highest value where all nodes synchronize. In both cases, the abrupt variations of the speed are canceled quickly for $r_c = 3$ as shown in Fig. 15(d), while for $r_c = 0.75$, the nodes speed diminishes slowly as σ_a increases [Fig. 15(c)]. Considering this sudden jump to $H_1 = H_{\max} \simeq 0.039$ in Figs. 15(a) and 15(b) and $V_1 \simeq 0.0011$ in Fig. 15(c), it comes out that all nodes in each layer flick from a low nonzero speed to a high-speed state to suddenly agglomerate and also stick themselves together in a rest position with a negligible speed. Thus we may conclude that, with an attractive coupling between

FIG. 13. Mutual influence of the couple (σ_a, r_c) on each layer. (a) Order parameter R_1 of layer 1; (b) interlayer error of synchronization E_{12}. Cyan shows the synchronous state and blue is the asynchronous state. The intralayer phase coupling is chosen $K_1 = K_2 = -0.1$ and the spatial one $J_1 = J_2 = 0.6$ with $\sigma_r = -0.1$ (see Fig. 9 in the supplemental material for the case of layer 2 [73]).
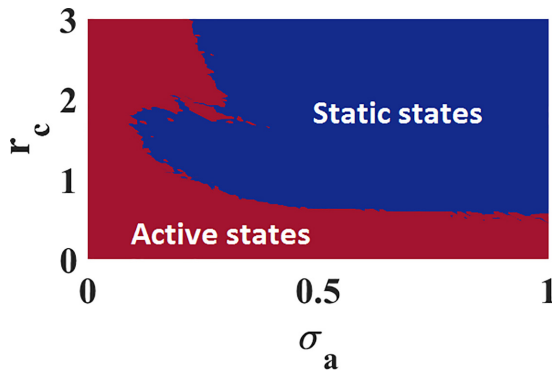

FIG. 12. Influence of attractive coupling σ_a and vision range r_c on each layer's active and static dynamics. Red shows the mean velocity of active states, $V_m \neq 0$, and blue the static ones, $V_m \approx 0$. The intralayer phase coupling is chosen as $K_1 = K_2 = -0.1$ and the spatial one $J_1 = J_2 = 0.6$ with $\sigma_r = -0.1$
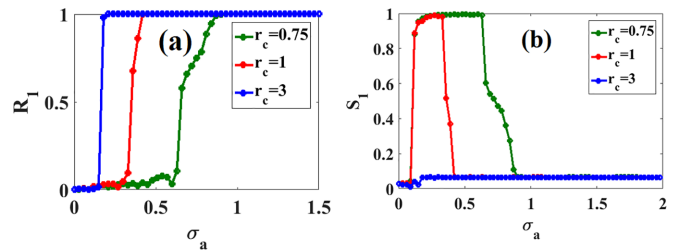

FIG. 14. (a) Order parameters R_1; (b) correlation S_1 of layer 1 as a function of the attractive coupling strength σ_a for different values of vision range r_c in the absence of repulsive coupling strength ($\sigma_r = 0$). Red is for $r_c = 1$, green for $r_c = 0.75$, and blue for $r_c = 3$. This was plotted for $K_1 = K_2 = -0.1$, $\sigma_r = 0$, $J_1 = J_2 = 0.1$ (see Fig. 10 in the supplemental material for the case of layer 2 [73])
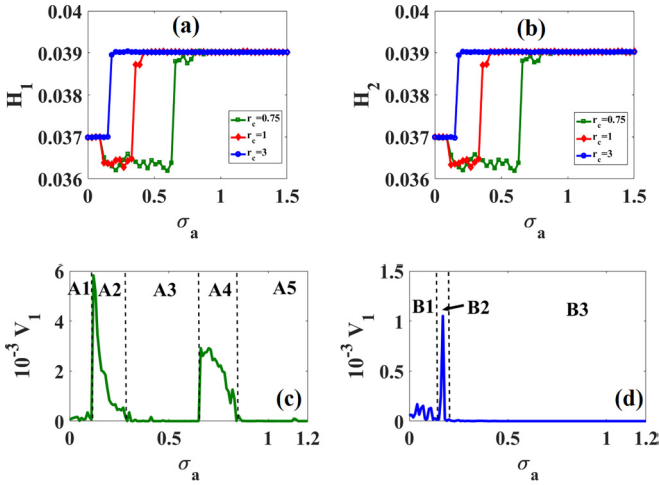
FIG. 15. Evolution of the mean energy and velocity of each layer as a function of the attractive coupling strength σ_a for different values of the vision range r_c. (a) Energy of layer 1; (b) energy of the layer 2; (c) mean velocity of the layer 1 for $r_c = 0.75$; and (d) mean velocity of the layer 1 for $r_c = 3$. Red is for $r_c = 1$, green for $r_c = 0.75$, and blue for $r_c = 3$; this was plotted for $K_1 = K_2 = -0.1$, $\sigma_r = 0$, $J_1 = J_2 = 0.1$.

two sets of swarmalators, if the vision range is large enough, then both layers could act as one single network and achieve explosive and long-range internal phase synchronization that defines a sharp high-speed transition to a sudden and static agglomeration state. In the (A2 and A3) area for lower values of r_c, the energy H_1 is almost at its lowest fluctuating value as well as the mean speed V_1. In these domains, an counterclockwise rotating wave appears that propagates on the θs, which is shown by the graphs in Fig. 16(a) for $\sigma_a = 0.25$ and by the video (see video 3 in the supplemental material [73]).

The region (A4) starts with the second jump, which is sudden, abrupt, and explosive but not strong enough to lead the nodes to complete synchronization. If we compare the mean speeds before the first and the second jumps in Fig. 15(c), then it is clear that the second transition is weaker as the swar-
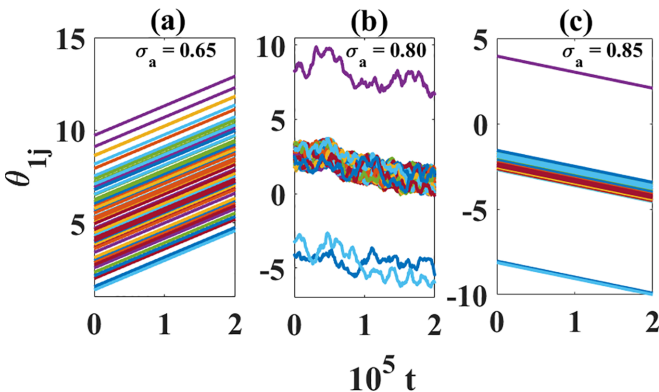

FIG. 16. Rotational waves. From the left to right (a) counterclockwise, $\sigma_a = 0.25$; (b) clockwise, $\sigma_a = 0.80$; and (c) $\sigma_a = 0.85$, respectively. The plot of this graph is done by using only the last 0.4 of the 5.10^5 total number of iterations. This is for $\sigma_r = 0$, $r_c = 0.75$, $K_1 = K_2 = -0.1$, $\sigma_r = 0$, $J_1 = J_2 = 0.1$ (video 3 and 4 in Ref. [73]).
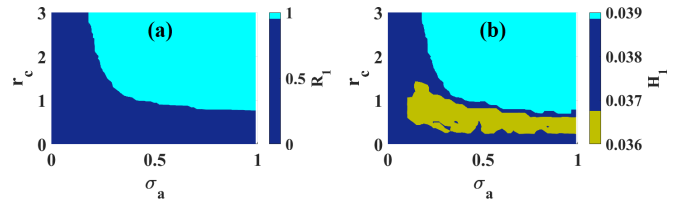

FIG. 17. Effect of (σ_a, r_c) on the transition to synchronization when $\sigma_r = 0$. (a) Order parameter R_1 of layer 1; (b) mean energy H_1 in layer 1. Cyan shows the synchronous state, blue is the asynchronous state, and the last, yellow, shows the intermediate state between the two transitions in the evolution of the mean energy. The intralayer phase coupling is chosen $K_1 = K_2 = -0.1$ and the spatial one $J_1 = J_2 = 0.1$ with $\sigma_r = 0$ (see Fig. 11 in the supplemental material [73] for the case of layer 2).

malators do not have enough energy since the speed before the second transition is very low. While in region (A3) the system rotates counterclockwise, during this transition, the coupled swarmalators perform an unstable clockwise rotating wave on the internal phase dynamics propagates in the opposite direction than that in Fig. 16(a) where the nodes' movement are essentially random even if the general motion seems to be a rotation [see Fig. 16(b)]. It seems as if the system uses the rotational wave as a way to save energy before the big jump to synchronization occurs, for $\sigma_a < 0.5$ (counterclockwise), and it also appears to use it to lose the speed it had acquired to jump (clockwise), in order to synchronize for $\sigma_a \approx 0.8$, where the random movement seems to have disappeared. The domain (A5) and (B3) are internal phase synchronization zones where all the nodes are progressively sticking themselves together and form one body in each layer as the value of σ_a increases. Hence, the entire system achieves a sudden and long-range internal phase synchronization.

From the description of Figs. 15 and 16, we partially conclude that in the absence of the repulsive coupling, namely $\sigma_r \to 0$ and for $r_c \leqslant r_{\text{critic}}$ where r_{critic} is the critical value below which the energy presents the drop, internal phase synchronization occurs in two steps: The first one corresponds to the domains (A2) and (A3) and the second one to (A4) and (A5). The first step [(A2) and (A3)] corresponds to the loss of motion in space but with the appearance of a rotational wave that propagates on the θ_js in an counterclockwise direction as shown in Fig. 16(a) (see the video 3 in the supplemental material [73]). The second step [(A4) and (A5)] corresponds to the increase of the energy until it progressively reaches its maximum $H_1 \simeq 0.039$. The jump and the convergence to phase synchronization pass through perturbed (with space agitation) and unperturbed (and static in space) rotational waves that propagate on the θ_js and move in a clockwise direction as shown in Figs. 16(b) and 16(c) (see the video 4 in the supplemental material [73]).

Varying r_c and σ_a simultaneously gives us the graphs shown in Fig. 17. Figure 17(a) shows the internal phases order parameter R_1 that shows two domains: a blue area where there is phase decoherence and the phase synchronization in the cyan region. On the other hand, Fig. 17(b) presents three different domains, which are defined as follows: phase decoherence in the blue area and phase synchronization in
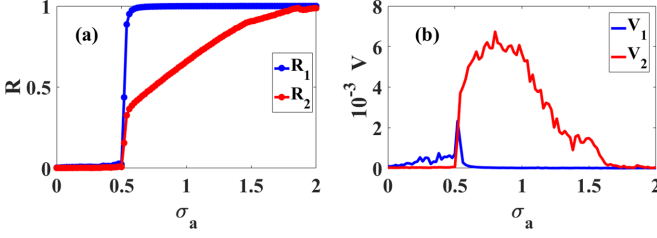
FIG. 18. Effect of internal dynamics (intraphase coupling $K_1 \neq K_2$) on the existence of explosive synchronization in the absence of interlayer repulsive coupling σ_r [see Eq. (7)]. (a) Order parameter of each layers R_1 and R_2; (b) mean velocity V_1 and V_2. The red is for the second layer and the blue for the first layer and the results are obtained for $J_1 = J_2 = 0.1$, $K_1 = -0.1$, $K_2 = -1$, $r_c = 3$ corresponding to the internal SpPW state in layer 1 and SA in layer 2. If we switch the values of K_1 and K_2, then the behaviors of the layers will simply switch also as seen in Fig. 12 in the supplemental material [73].

the cyan space; meanwhile, H_1 decreases suddenly in the yellow region. Comparing both Figs. 12 and 17, we see that the synchronization domain is larger in Fig. 17 than in Fig. 12 due to the value of the repulsive coupling $\sigma_r = 0$ and $\sigma_r = -0.1$, respectively, with equal values for the other parameters.

Let us recall that for $K_1 = K_2 = -0.1$, the coupled swarmalators displayed an explosive phase synchronization (see Figs. 14 and 15). Therefore, in what follows, the goal is to look at how the intralayer coupling K_m, with $m = 1, 2$ for the first and second layers respectively, can change the dynamics for $r_c = 3$. The graphs on Fig. 18 give the behaviors of both swarmalators for $J_1 = J_2 = 0.1$, $K_1 = -0.1$, $K_2 = -1$, and $r_c = 3$. It occurs that for these values, the first layer is achieving an explosive synchronization while the second is moving progressively to the synchronization state [see the graphs in Figs. 18(a) and 18(b)]. These figures switch colors when we exchange K_1 and K_2.

V. STABILITY ANALYSIS OF THE COUPLED LAYERS

This section is devoted to analyzing the global stability of the system constituted by two coupled networks of swarmalators, as expressed through Eqs. (5), (6), and (7). The attractive and repulsive couplings are supposed not null to figure out a more general expression. Thus, for a considered layer m and chosen nodes i and j and $\theta_i^l - \theta_i^m$ and $\theta_j^m - \theta_i^m$ near zero, regardless of the values of l and m taken between 1 or 2, meaning near synchronization, the expression of the time derivative of θ_i^m is given as follows:

$$\dot{\theta}_i^m = \frac{K_m}{N} \sum_j^N \frac{\varepsilon_j^m}{|r_{ij}^m|} + \frac{\sigma_a}{N_a^m} \sum_j^N \frac{\varepsilon_j^{lm}}{D_{ij}^m} + \frac{\sigma_r}{N_r^m} \sum_j^N \frac{\varepsilon_j^{lm}}{D_{ij}^m}, \quad (34)$$

where the error between two random internal phases located at layers l and m is defined as $\varepsilon_j^{lm} = \theta_j^l - \theta_i^m$; for the same layer the error is defined as $\varepsilon_j^m = \theta_j^m - \theta_i^m$ and the distance between two elements from the same layer is given as $r_{ij}^m = X_j^m - X_i^m$. For clarity, θ_i^1 and θ_i^2 are chosen to investigate the conditions that lead the entire system to stability. It follows that the error

between both layers is expressed as

$$\varepsilon_i^{21} = \theta_i^2 - \theta_i^1, \quad (35)$$

and its time derivative is given by the following relation:

$$\dot{\varepsilon}_i^{21} = \frac{K}{N} \sum_j^N \left(\frac{\varepsilon_j^2}{|r_{ij}^2|} - \frac{\varepsilon_j^1}{|r_{ij}^1|} \right) + \frac{\sigma_a}{N_a^2} \sum_j^N \frac{\varepsilon_j^{12}}{D_{ij}^2} - \frac{\sigma_a}{N_r^1} \sum_j^N \frac{\varepsilon_j^{21}}{D_{ij}^1}$$

$$+ \frac{\sigma_r}{N_a^2} \sum_j^N \frac{\varepsilon_j^{12}}{D_{ij}^2} - \frac{\sigma_r}{N_r^1} \sum_j^N \frac{\varepsilon_j^{21}}{D_{ij}^1}. \quad (36)$$

From the fact that $\varepsilon_j^2 - \varepsilon_j^1 = \varepsilon_j^{21} - \varepsilon_i^{21}$, Eq. (36) can be rewritten as

$$\dot{\varepsilon}_i^{21} = \frac{K}{N} \sum_j^N \left[\frac{\varepsilon_j^{21} - \varepsilon_i^{21}}{|r_{ij}^2|} + \varepsilon_j^1 \left(\frac{1}{|r_{ij}^2|} - \frac{1}{|r_{ij}^1|} \right) \right]$$

$$+ \sigma_a \left[\frac{1}{N_a^2} \sum_j^N \frac{\varepsilon_j^{12}}{D_{ij}^2} - \frac{1}{N_a^1} \sum_j^N \frac{\varepsilon_j^{21}}{D_{ij}^1} \right]$$

$$+ \sigma_r \left[\frac{1}{N_r^2} \sum_j^N \frac{\varepsilon_j^{12}}{D_{ij}^2} - \frac{1}{N_r^1} \sum_j^N \frac{\varepsilon_j^{21}}{D_{ij}^1} \right]. \quad (37)$$

From Eq. (37), a candidate Lyapunov function can be expressed as

$$Q_i = \tfrac{1}{2} \left(\varepsilon_i^{21} \right)^2 \quad (i = 1, \ldots, N), \quad (38)$$

and its time derivative is given by the following expression:

$$\dot{Q}_i = \frac{K}{N} \sum_j^N \left[\frac{\varepsilon_j^{21} \varepsilon_i^{21} - \varepsilon_i^{21} \varepsilon_i^{21}}{|r_{ij}^2|} + \varepsilon_j^1 \varepsilon_i^{21} \left(\frac{1}{|r_{ij}^2|} - \frac{1}{|r_{ij}^1|} \right) \right]$$

$$+ \sigma_a \left[\frac{1}{N_a^2} \sum_j^N \frac{\varepsilon_j^{12} \varepsilon_i^{21}}{D_{ij}^2} - \frac{1}{N_a^1} \sum_j^N \frac{\varepsilon_j^{21} \varepsilon_i^{21}}{D_{ij}^1} \right]$$

$$+ \sigma_r \left[\frac{1}{N_r^2} \sum_j^N \frac{\varepsilon_j^{12} \varepsilon_i^{21}}{D_{ij}^2} - \frac{1}{N_r^1} \sum_j^N \frac{\varepsilon_j^{21} \varepsilon_i^{21}}{D_{ij}^1} \right]. \quad (39)$$

From relation Eq. (39), it is clear that the first condition for stability is to have $\varepsilon_j^1 = 0$; namely, in order to have complete internal phase synchronization, each swarmalator should first achieve intralayer synchronization. From the relations $\varepsilon_j^{21} = -\varepsilon_j^{12}$ and $a.b \leqslant \frac{a^2 + b^2}{2}$ Eq. (39) becomes

$$\dot{Q}_i \leqslant \sum_j^N \frac{K}{N} \left[\frac{\left(\varepsilon_j^{21} \right)^2 + \left(\varepsilon_i^{21} \right)^2}{2 |r_{ij}^2|} \right] - \left(\varepsilon_i^{21} \right)^2 \frac{K}{N} \frac{1}{|r_{ij}^2|}$$

$$+ \sigma_a \sum_J^N \left[\frac{1}{N_a^2} \frac{\left(\varepsilon_j^{12} \right)^2 + \left(\varepsilon_i^{21} \right)^2}{2 D_{ij}^2} + \frac{1}{N_a^1} \frac{\left(\varepsilon_j^{21} \right)^2 + \left(\varepsilon_i^{21} \right)^2}{2 D_{ij}^1} \right]$$

$$+ |\sigma_r| \sum_j^N \left[\frac{1}{N_r^2} \frac{\left(\varepsilon_j^{12} \right)^2 + \left(\varepsilon_i^{21} \right)^2}{2 D_{ij}^2} + \frac{1}{N_r^1} \frac{\left(\varepsilon_j^{21} \right)^2 + \left(\varepsilon_i^{21} \right)^2}{2 D_{ij}^1} \right]$$
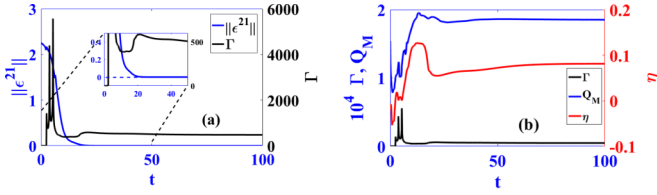
$$(40)$$

FIG. 19. Global stability analysis. (a) Convergence of the mean error; (b) stability condition. In (a), we have the mean error $\|\varepsilon^{21}\|$ (blue) and Γ (black) and in (b) η in (red) and Q_M in (blue). This was plotted with $J = 0.1$, $K_1 = K_2 = -0.1$, $\sigma_a = 0.9$, $\sigma_r = 0$, and $r_c = 2.5$.

$$\dot{Q}_i \leqslant \left(\varepsilon_i^{21}\right)^2 \sum_j^N \left[\begin{array}{c} \frac{K}{2N|r_{ij}^2|} - \frac{K}{N|r_{ij}^2|} + \frac{\sigma_a}{N_a^2}\frac{1}{2D_{ij}^2} \\ + \frac{\sigma_a}{N_a^1}\frac{1}{2D_{ij}^1} + \frac{|\sigma_r|}{N_r^2}\frac{1}{2D_{ij}^2} + \frac{|\sigma_r|}{N_r^1}\frac{1}{2D_{ij}^1} \end{array} \right]$$
$$+ \sum_j^N \left[\begin{array}{c} \frac{K}{N}\frac{(\varepsilon_j^{12})^2}{2|r_{ij}^2|} + \frac{\sigma_a}{N_a^2}\frac{(\varepsilon_j^{12})^2}{2D_{ij}^2} + \frac{\sigma_a}{N_a^1}\frac{(\varepsilon_j^{12})^2}{2D_{ij}^1} \\ + \frac{|\sigma_r|}{N_r^2}\frac{(\varepsilon_j^{12})^2}{2D_{ij}^2} + \frac{|\sigma_r|}{N_r^1}\frac{(\varepsilon_j^{12})^2}{2D_{ij}^1} \end{array} \right]. \quad (41)$$

Maximizing the distance between entities inside each layer and minimizing the distance between those in opposite layers, there exist positive constants $\chi_{\min}$, $\chi_{\max}$, and D_0 (with D_0 being the smallest distance between swarmalators even if the layers collapse, $d_0 = 0$) such that

$\chi_{\min} \leqslant r_{ij}^m \leqslant \chi_{\max}$ and $\min(D_{ij}^m) \geqslant D_0$

$$\dot{Q}_i \leqslant \left(\varepsilon_i^{21}\right)^2 \left[-\frac{K}{\chi_{\max}} + \frac{K}{2\chi_{\min}} + \frac{\sigma_a}{2D_0}C_1 + \frac{|\sigma_r|}{2D_0}C_2 \right]$$
$$+ Q\left(\varepsilon_j^{12}\right) \quad (42)$$

with

$$C_1 = \left(\frac{N}{N_a^2} + \frac{N}{N_a^1} \right) \quad \text{and} \quad C_2 = \left(\frac{N}{N_r^2} + \frac{N}{N_r^1} \right) \quad (43)$$

$$Q\left(\varepsilon_j^{12}\right) = \sum_j^N \left(\varepsilon_j^{12}\right)^2 \left[\begin{array}{c} \frac{K}{2N\chi_{\min}} + \frac{\sigma_a}{2D_0 N_a^2} + \frac{\sigma_a}{2D_0 N_a^1} \\ + \frac{|\sigma_r|}{2D_0 N_r^2} + \frac{|\sigma_r|}{2D_0 N_r^1} \end{array} \right]. \quad (44)$$

Let $C_0 = \max(C_1, C_2)$; for $K(\frac{2\chi_{\min} - \chi_{\max}}{2\chi_{\min}\chi_{\max}}) \geqslant \frac{C_0\chi_{\max}}{D_0}$ $(\sigma_a + |\sigma_r|)$ Eq. (42) can be rewritten as

$$\dot{Q}_i \leqslant -\eta\left(\varepsilon_i^{21}\right)^2 + Q_M, \quad (45)$$

where $\eta = K(\frac{2\chi_{\min} - \chi_{\max}}{2\chi_{\min}\chi_{\max}}) - \frac{C_0}{2D_0}(\sigma_a + |\sigma_r|)$ and $Q_M = \max(Q(\varepsilon_j^{12}))$. It follows that, if $\|\varepsilon_i^{21}\| > \sqrt{\frac{Q_M}{\eta}}$, then $\dot{Q}_i < 0$. Hence Q decreases with $\|\varepsilon_i^{21}\|$ [see Eq. (38)]. Thus, from the standard invariance arguments, it comes that the error satisfies asymptotically the following bound, which is defined as

$$\left\|\varepsilon_i^{21}\right\| \leqslant \Gamma, \quad (46)$$

where $\Gamma \geqslant \sqrt{\frac{Q_M}{\eta}}$. According to Kakmeni *et al.* [74], this achieves the proof.

In order to verify the main condition [Eq. (46)] to achieve asymptotic stability, Figs. 19(a) and 19(b) show the convergence of the mean error $\|\varepsilon^{21}\|$, the constant variation η, and Q_M described respectively in Eqs. (35), (44), and (45). For this

representation, we have considered the parameters of Fig. 17 where synchronization appears (see cyan domain): $\sigma_r = 0$, $\sigma_a = 0.9$ and $r_c = 2.5$. The main observation of these figures is the fact that stability between the two layers is obtained when the condition of Eq. (46) is respected where η should be positive [see Fig. 19(a)]. Also, the maximization of Q_M comes with the minimization of the distances D_{ij}^m ($m = 1, 2$), $\chi_{\min}$ and $\chi_{\max}$ to the smallest value of r_{ij}^m that is reached at the synchronization. This allows us to clearly show that the mean error becomes bounded by Γ and converge to zero when the stability is reached around $t = 20$.

VI. CONCLUSION

This work investigated the dynamics of coupled swarmalators with attractive and repulsive coupling. The first type applies to nodes within a domain defined by a vision range r_c, while the second applies to those outside the vision range. A study of the system's dynamics as a function of the vision range showed a richness of phase dynamics, such as the formation of clusters, synchronization, and antiphase synchronization. Increasing the vision range gave way to the formation of static dynamics of the entities (SS, SA, and SPW), while its decrease favored that of active dynamics (SpPW and APW). A detailed study of the phases is presented in Sec. IV A. In addition to these dynamics, the ISSPI state was highlighted. The study of the stability of this state in the sense of Lyapunov was done, which showed us that the phase synchronization obtained is locally stable. This stability study was extended to the two layers independently of their internal dynamics. In contrast to the attractive coupling, the influence of the repulsive coupling seems to delay the phase synchronization between the entities. Analysis of the energy of the phases showed a surprising richness of transitions, as a function of σ_a and r_c, until the systems reach complete internal phase synchronization. We observe first- and second-order transitions and the appearance of internal phases rotating waves preceding explosive behavior and complete synchronization.

ACKNOWLEDGMENTS

APPENDIX: GLOSSARY

AMPW: attractive mixed phase wave
APW: active phase wave
ISSPI: interlayer static sync π
RMPW: repulsive mixed phase wave
SA: static async
SCS: static cluster sync
SPI: static π
SpPW: splintered phase wave
SPW: static phase wave
SS: static sync

[1] L. Bauer, J. Bassett, P. Hövel, Y. N. Kyrychko, and K. B. Blyuss, Chaos **27**, 114317 (2017).

[2] S. Samatas and J. Lintuvuori, Phys. Rev. Lett. **130**, 024001 (2023).

[3] S. Majhi, B. K. Bera, D. Ghosh, and M. Perc, Phys. Life Rev. **28**, 100 (2019).

[4] T. A. Glaze, S. Lewis, and S. Bahar, Chaos **26**, 083119 (2016).

[5] R. Dariani, A. Buscarino, L. Fortuna, and M. Frasca, Complex Syst. **20**, 279 (2011).

[6] I. Ormazábal, F. Urbina, F. A. Borotto, and H. F. Astudillo, Phys. Rev. E **105**, 054110 (2022).

[7] P. Louodop, S. Saha, R. Tchitnga, P. Muruganandam, S. K. Dana, and H. A. Cerdeira, Phys. Rev. E **96**, 042210 (2017).

[8] T. Njougouo, V. Camargo, P. Louodop, F. F. Ferreira, P. K. Talla, and H. A. Cerdeira, Chaos **30**, 123136 (2020).

[9] T. Njougouo, G. R. Simo, P. Louodop, H. Fotsin, and P. K. Talla, Chaos Solitons Fract **139**, 110082 (2020).

[10] C. Huygens, Letters to de Sluse, (letters; no. 1333 of 24 February 1665, no. 1335 of 26 February 1665, no. 1345 of 6 March 1665) (Societe Hollandaise Des Sciences, Martinus Nijho, (1895).

[11] H. D. Abarbanel, M. I. Rabinovich, A. Selverston, M. V. Bazhenov, R. Huerta, M. M. Sushchik, and L. L. Rubchinskii, Phys. Usp. **39**, 337 (1996).

[12] R. E. Mirollo and S. H. Strogatz, SIAM J. Appl. Math. **50**, 1645 (1990).

[13] J. K. Jang, A. Klenner, X. Ji, Y. Okawachi, M. Lipson, and A. L. Gaeta, Nat. Photon **12**, 688 (2018).

[14] K. P. O'Keeffe, H. Hong, and S. H. Strogatz, Nat. Commun. **8**, 1504 (2017).

[15] A. Barciś and C. Bettstetter, IEEE Access **8**, 218752 (2020).

[16] J. U. F. Lizarraga and M. A. M. de Aguiar, Chaos **30**, 053112 (2020).

[17] V. Nguefoue, T. Njougouo, P. Louodop, H. Fotsin, and H. A. Cerdeira, Eur. Phys. J. Spec. Top. **231**, 237 (2022).

[18] G. K. Sar, S. N. Chowdhury, M. Perc, and D. Ghosh, New J. Phys. **24**, 043004 (2022).

[19] G. R. Simo, P. Louodop, D. Ghosh, T. Njougouo, R. Tchitnga, and H. A. Cerdeira, Phys. Lett. A **409**, 127519 (2021).

[20] G. R. Simo, T. Njougouo, R. P. Aristides, P. Louodop, R. Tchitnga, and H. A. Cerdeira, Phys. Rev. E **103**, 062304 (2021).

[21] L. M. Pecora and T. L. Carroll, Phys. Rev. Lett. **64**, 821 (1990).

[22] M. G. Rosenblum, A. S. Pikovsky, and J. Kurths, Phys. Rev. Lett. **76**, 1804 (1996).

[23] W. Yang, X. Xia, Y. Dong, and S. Zheng, Comput. Inf. Sci. **3**, 174 (2010).

[24] M. P. Aghababa, Chin. Phys. B **21**, 030502 (2012).

[25] A. M. B. Lashiher and C. Storey, J. Inst. Math. Appl. **9**, 397 (1972).

[26] L. Lam and L. Weiss, J. Frankl. Inst. **298**, 415 (1975).

[27] I. G. Da Silva, J. M. Buldú, C. R. Mirasso, and J. García-Ojalvo, Chaos **16**, 043113 (2006).

[28] R. Kengne, R. Tchitnga, A. Mezatio, A. Fomethe, and G. Litak, Eur. Phys. J. B **90**, 88 (2017).

[29] P. Louodop, H. Fotsin, M. Kountchou, Elie B. Megam Ngouonkadi, H. A. Cerdeira, and S. Bowong, Phys. Rev. E **89**, 032921 (2014).

[30] P. Louodop, M. Kountchou, H. Fotsin, and S. Bowong, Nonlin. Dynam. **78**, 597 (2014).

[31] N. Fujiwara, J. Kurths, and A. Díaz-Guilera, Phys. Rev. E **83**, 025101(R) (2011).

[32] M. Frasca, A. Buscarino, A. Rizzo, L. Fortuna, and S. Boccaletti, Phys. Rev. E **74**, 036110 (2006).

[33] M. Frasca, A. Buscarino, A. Rizzo, L. Fortuna, and S. Boccaletti, Phys. Rev. Lett. **100**, 044102 (2008).

[34] S. Meloni, A. Buscarino, L. Fortuna, M. Frasca, J. Gómez-Gardenes, V. Latora, and Y. Moreno, Phys. Rev. E **79**, 067101 (2009).

[35] S. Majhi, D. Ghosh, and J. Kurths, Phys. Rev. E **99**, 012308 (2019).

[36] K. P. O'Keeffe and C. Bettstetter, *Micro-and Nanotechnology Sensors, Systems, and Applications XI*, Vol. 10982 (International Society for Optics and Photonics, Bellingham, WA 2019), 109822E.

[37] K. P. O'Keeffe, J. H. M. Evers, and T. Kolokolnikov, Phys. Rev. E **98**, 022203 (2018).

[38] H. K. Lee, K. Yeo, and H. Hong, Chaos **31**, 033134 (2021).

[39] J. Gómez-Gardeñes, S. Gómez, A. Arenas, and Y. Moreno, Phys. Rev. Lett. **106**, 128701 (2011).

[40] X. Zhang, S. Boccaletti, S. Guan, and Z. Liu, Phys. Rev. Lett. **114**, 038701 (2015).

[41] A. D. Kachhvah and S. Jalan, Europhys. Lett. **119**, 60005 (2017).

[42] I. Leyva, A. Navas, I. Sendiña-Nadal, J. A. Almendral, J. M. Buldú, M. Zanin, D. Papo, and S. Boccaletti, Sci. Rep. **3**, 1281 (2013).

[43] S. Boccaletti, J. A. Almendral, S. Guan, I. Leyva, Z. Liu, I. Sendiña-Nadal, Z. Wang, and Y. Zou, Phys. Rep. **660**, 1 (2016).

[44] H. Hong and E. A. Martens, Chaos **32**, 063125 (2022).

[45] P. S. Skardal and A. Arenas, Phys. Rev. E **89**, 062811 (2014).

[46] S. Jalan, V. Rathore, and A. Deep Kachhvah, and A. Yadav, Phys. Rev. E **99**, 062305 (2019).

[47] S. Jalan, A. D. Kachhvah, and H. Jeong, J. Comput. Sci. **46**, 101177 (2020).

[48] T. Wu, S. Huo, K. Alfaro-Bittner, S. Boccaletti, and Z. Liu, Phys. Rev. Res. **4**, 033009 (2022).

[49] M. Aldana, H. Larralde, and B. Vázquez, Int. J. Mod. Phys. B **23**, 3661 (2009).

[50] H. Christodoulidi, K. van der Weele, Ch. G. Antonopoulos, and T. Bountis, *Chaos, Information Processing and Paradoxical Games: The Legacy of John S Nicolis* (World Scientific, Singapore, 2015), pp. 383–398.

[51] A. Attanasi, A. Cavagna, L. Del Castello, I. Giardina, J. Asja, S. Melillo, L. Parisi, O. Pohl, E. Shen, and M. Viale, J. R. Soc. Interface **12**, 20150319 (2015).

[52] T. M. Winsor, The Auk **32**, 198 (1915).

[53] S. Bahar, *The Essential Tension: Competition, Cooperation and Multilevel Selection in Evolution* (Springer, Berlin, 2018), pp. 127–152.

[54] J. Buhl, D. J. T. Sumpter, I. Couzin, J. Hale, E. Despland, E. R. Miller, and S. J. Simpson, Science **312**, 1402 (2006).

[55] M. Beekman, D. J. T. Sumpter, and F. L. W. Ratnieks, Proc. Natl. Acad. Sci. U.S.A. **98**, 9703 (2001).

[56] E. F. W. Heffern, H. Huelskamp, S. Bahar, and R. F. Inglis, Proc. R. Soc. B **288**, 20211111 (2021).

[57] S. Ghosh, A. Zakharova, and S. Jalan, Chaos Solitons Fract. **106**, 56 (2018).

[58] J. Sawicki, I. Omelchenko, A. Zakharova, and E. Schöll, Eur. Phys. J. Spec. Top. **227**, 1161 (2018).

[59] J. Sawicki, S. Ghosh, S. Jalan, and A. Zakharova, Front. Appl. Math. Stat. **5**, 19 (2019).

[60] M. Winkler, J. Sawicki, I. Omelchenko, A. Zakharova, V. Anishchenko, and E. Schöll, Europhys. Lett. **126**, 50004 (2019).

[61] S. Makovkin, A. Kumar, A. Zaikin, S. Jalan, and M. Ivanchenko, Phys. Rev. E **96**, 052214 (2017).

[62] S. Jalan and A. Singh, Europhys. Lett. **113**, 30002 (2016).

[63] I. Leyva, I. Sendiña-Nadal, R. Sevilla-Escoboza, V. P. Vera-Avila, P. Chholak, and S. Boccaletti, Sci. Rep. **8**, 8629 (2018).

[64] E. Rybalova, G. Strelkova, E. Schöll, and V. Anishchenko, Chaos **30**, 061104 (2020).

[65] S. K. Dwivedi, M. S. Baptista, and S. Jalan, Phys. Rev. E **95**, 040301(R) (2017).

[66] M. F. Copeland and B. D. Weibel, Soft Matter **5**, 1174 (2009).

[67] J. M. Swiecicki, O. Sliusarenko, and D. B. Weibel, Integr. Biol. **5**, 1490 (2013).

[68] L. D. Renner and D. B. Weibel, MRS Bull. **36**, 347 (2011).

[69] H. Hong, K. Yeo, and H. K. Lee, Phys. Rev. E **104**, 044214 (2021).

[70] F. Jiménez-Morales, Phys. Rev. E **101**, 062202 (2020).

[71] Y. Kuramoto and D. Battogtokh, Nonlin. Phenom. Complex Syst. **5**, 380 (2002).

[72] H. Hong, Chaos **28**, 103112 (2018).

[73] See Supplemental Material at http://link.aps.org/supplemental/10.1103/PhysRevE.108.034303 for some additional figures of the dynamics of the layer 2 and the video of SCS, the ISSPI state, and rotational wave transition to synchronization.

[74] F. M. M. Kakmeni, S. Bowong, D. V. Senthikumar, and J. Kurths, Chaos **20**, 043121 (2010).

[75] M. Sekieta and T. Kapitaniak, Int. J. Bifurcat Chaos **06**, 1901 (1996).

[76] R. Femat and G. Solís-Perales, Phys. Rev. E **65**, 036226 (2002).

[77] J. M. Kosterlitz and D. J. Thouless, J. Phys. C: Solid State Phys. **6**, 1181 (1973).

[78] N. Bhadra and S. K. Patra, Mod. Phys. Lett. B **32**, 1850147 (2018).